PCCP

Accepted Manuscript

ROYAL SOCIETY OF CHEMISTRY

www.rsc.org/pccp

Phys. Chem. Chem. Phys.

RSCPublishing

ARTICLE

Extinction and extra-high depolarized light scattering spectra of gold nanorods with improved purity and dimension tunability: direct and inverse problems

Cite this: DOI: 10.1039/x0xx00000x

Received 00th December 2013,
Accepted 00th January 2014

DOI: 10.1039/x0xx00000x

www.rsc.org/

Boris N. Khlebtsov,[a,b] Vitaly A. Khanadeev,[a,b] and Nikolai G. Khlebtsov[a,b,*]

The experimental depolarized light scattering ratio I_{VH}/I_{VV} from plasmonic nanorods is strongly decreased by a co-polarized contribution from impurity particles inevitably presented in suspensions fabricated by common seed-mediated methods with a single surfactant [typically, hexadecyltrimethylammonium bromide (CTAB)]. We used a binary NaOL (sodium oleate) + CTAB surfactant method (Ye et al., Nano Lett. 2013, 13, 555) to dramatically decrease the percentage of impurity particles in suspensions of as-prepared and overgrown nanorods without any separation procedures. The as-prepared nanorods demonstrated a very high ratio of longitudinal to transversal plasmonic maxima (of about 7) and an unprecedented, extra-high depolarized light scattering ratio I_{VH}/I_{VV} (of about 60%). To the best of our knowledge, this is the first experimental demonstration of the depolarized light scattering ratio approaching the theoretical limit of 75%. The NaOL+CTAB growing solution was also used to increase the nanorod diameters and lengths by a controllable overgrowing process. Statistical TEM data for as-prepared and overgrown nanorods were used to solve a direct problem, i.e. for T-matrix simulation of the extinction and depolarized light scattering spectra. To solve an inverse problem, with the extinction peak wavelength and full width at half-maximum (FWHM) as the input parameters, we obtained calibration plots to quantify the aspect ratio distribution in terms of a simple two-parametric log-normal model. Simultaneous fitting of the T-matrix calculations of extinction and depolarized light scattering spectra to the experimental data enabled us to retrieve the aspect ratio distribution and the percentage of impurity particles, in excellent agreement with statistical estimations based on transmission electron microscopy images.

1. Introduction

Gold nanorods (GNRs) have attracted significant attention owing to their promising applications in nanoplasmonics and nanophotonics,[1] chemical and bioanalytical sensing,[2] surface enhanced Raman spectroscopy,[3] and biomedicine.[4,5] For a detailed discussion of the synthesis, functionalization, characterization, plasmonic properties, and applications of GNRs, the readers are referred to an excellent recent review by Wang and co-workers.[6]

Owing to the intrinsic shape anisotropy and excitation of longitudinal and transversal localized plasmon resonances (LPRs), GNRs possess remarkable optical anisotropic properties,[7] which have been explored in liquid-crystal technologies,[8,9] conversion of light polarization,[10] five-dimensional optical recording,[11] and chemical sensing.[12] By contrast to scattering from spheres,[13,14] there also exists significant depolarization of light scattered by randomly oriented GNRs[15,16] and silver nonspherical particles.[17] Furthermore, mechanical[18] or electrical[19] alignment of GNRs or Ag/SiO_2 composites[20] results in enhanced anisotropic optical properties such as depolarization, dichroism, and birefringence. The sensitivity of depolarized light scattering to deviation of the particle shape from sphericity has been utilized as a convenient test in the ensemble[21] and single-particle[22] shape characterization, and also for tracking nonspherical nanoparticles within living cells.[23]

If a suspension of GNRs is illuminated by linearly polarized light, the cross-polarized scattering intensity (at 90 degrees) I_{VH} occurs, whereas for spheres, the depolarization ratio $\Delta_{VH} = I_{VH} / I_{VV}$ equals zero. Here, the subscripts "*V*" and "*H*" stand for vertical and horizontal polarization with respect to the scattering plane. One of the main challenges in experimental measurements of Δ_{VH} is the co-polarized contribution I^*_{VV} from impurity particles to the co-polarized intensity I_{VV} from GNRs. Various quasi-spherical, cubical, and platelet impurity particles are typical of all CTAB-assisted seed-mediated fabrication protocols.[24] This great flexibility of nanoparticle shapes results from overgrow processes, according to an evolutionary tree of morphologies displaying a library of nanoparticles grown from the seeds.[25]

The second challenging issue is related to the low scattered intensities at the depolarization maximum wavelength. Indeed, experimental measurements and T-matrix calculations[16] show that the depolarization ratio maximum wavelength ($\lambda_{VH}^{\max}$) is located between longitudinal ($\lambda_{\parallel}^{\max}$) and transversal ($\lambda_{\perp}^{\max}$) plasmonic extinction peaks, typically between 620 and 650 nm. Accordingly, the co-polarized and cross-polarized intensities can be rather small in comparison with their plasmonic resonance values. This means that the measured depolarization ratio $\Delta_{VH} = I_{VH} / (I_{VV} + I_{VV}^{*})$ can be strongly decreased even if the percentage of quasi-spherical impurity particles is small enough. Although several separation procedures have been developed to improve the purity of GNR samples,[26,27] they are time-consuming and do not solve all experimental problems.

Recently, Murray and co-workers reported a new method for GNR fabrication that is based on the binary NaOL (sodium oleate) + CTAB surfactant mixture.[28] In this paper, we used the binary surfactant method[28] to dramatically decrease the percentage of impurity quasi-spherical particles in as-prepared nanorod samples (less than 3%) without any separation procedures. With these high quality samples, we observed, for the first time, an unprecedented depolarized light scattering ratio of about 60%, located near 620 nm, whereas the major plasmonic resonance was observed at 960 nm. Furthermore, the same mixture-growing solution and NaOL + CTAB fabricated GNRs were used to increase the nanorod diameter and length by a controllable overgrowing process. Transmission electron microscopy (TEM) data for as-prepared and overgrown nanorods were used for the T-matrix simulation of extinction and depolarized light scattering spectra, i.e. for the solution of a direct light scattering problem. We also provide calibration plots for determining the aspect ratio distribution (in terms of a simple two-parametric log-normal model), with the extinction peak wavelength and full width at half-maximum (FWHM) as input parameters. By simultaneous fitting of the T-matrix extinction and depolarized light scattering spectra to the experimental spectra, we were able to retrieve the aspect ratio distribution of GNRs and the average percentage of impurity particles, in excellent agreement with the statistical estimations based on TEM images.

2. Experimental procedures and theoretical models

2.1. Materials

All chemicals were obtained from commercial suppliers and used without further purification. Hexadecyltrimethylammonium bromide (CTAB, > 98.0%), sodium oleate (NaOL, technical grade, > 82% fatty acid), L-ascorbic acid (AA, >99,9%), hydrochloric acid (HCl, 37 wt. % in water), and sodium borohydride ($NaBH_4$, 99%) were purchased from Sigma-Aldrich. Hydrogen tetrachloroaurate trihydrate ($HAuCl_4 \cdot 3H_2O$) and silver nitrate ($AgNO_3$, >99%) were purchased from Alfa Aesar. Ultrapure water obtained from a Milli-Q Integral 5 system was used in all experiments.

2.2. Synthesis and overgrowth of GNRs

Synthesis of GNRs and their overgrowth in NaOL–CTAB is described in detail elsewhere.[29] In brief, a 2–3 nm seed solution was first prepared by adding 0.025 mL of 10 mM $HAuCl_4$ to 1 mL of aqueous 0.1 M CTAB. This was followed by adding 1 mL of 10 mM $NaBH_4$ and by aging at room temperature for 30 min before use in the next step. For preparing the growth solution, 7.0 g of CTAB and 1.234 g of NaOL were dissolved in 250 mL of warm water (~50 °C). The solution was allowed to cool to 30 °C, and 18 mL of 4 mM $AgNO_3$ was added. The mixture was kept undisturbed at 30 °C for 15 min, after which 250 mL of 1 mM $HAuCl_4$ was added. The solution became colourless after 90 min of stirring, indicating the reduction of Au^{3+} to Au^{+}. The pH of the growth solution was adjusted by adding 2.1 mL of HCl (37 wt. %). After another 15 min, 1.25 mL of 64 mM ascorbic acid and 0.8 mL of the seeds solution were added. The resultant mixture was left undisturbed at 30 °C for 48 h for NR growth. Typically, the zeta potential of as-prepared rods varied from +30 to +40 mV.

For the overgrowth process, 20 mL of the growth solution was mixed with an appropriate amount (1 to 20 mL) of prepared nanorods to stimulate additional reduction of Au on the NR surface. The resultant mixtures were left undisturbed at 30 °C for 48 h.

2.3. Characterization of GNRs

TEM images of the nanoparticles were obtained with a Libra-120 transmission electron microscope (Carl Zeiss, Germany). Extinction spectra were recorded with a Specord BS-250 UV–vis spectrophotometer (Analytik Jena, Germany). The zeta potential of the particles was determined with a Zetasizer Nano-ZS instrument (Malvern, UK). GNR diameters and lengths were evaluated from digitized TEM images (Grapher 8, Golden Software, Inc.) of about 600 nanorods. The number percentage of impurity particles was evaluated from six overview TEM images (image sizes, 2.5×2.5 μm; scale bar, 500 nm) containing about 1000 particles each.

2.4. Depolarization measurements

Figure 1 shows a simplified scheme for the observation of depolarized light scattering (Fig. 1a) and the corresponding experimental setup (Fig. 1b) for measuring the co-polarized and cross-polarized light scattering intensities.[16] An achromatic lens (*2*) with a 50-mm focus length and with iris diaphragms (*3*) and (*5*) forms an enlarged image of a 15-W halogen lamp (*1*) filament near the centre of a four-sided 1-cm rectangular non-fluorescent-quartz cuvette (*7*). For spectral measurements, we used the interference filters (Oriel, USA, $\lambda_{\max} = 400 - 1000$ nm, $\Delta\lambda_{1/2,\max} = 5$ nm). Typically, the wavelength step was 20 nm. The incident and scattered light beams were polarized and analyzed with Glan–Thompson calcite prisms. An iris diaphragm (*9*) and an achromatic lens (*10*, 30-mm focal length) form an image of the scattering volume, which can be viewed by a spherical mirror (*11*) with a central pin hole (0.1, 0.5, and 1.5 mm) and an objective lens (*12*). The pin hole with a diameter of 0.1, 0.5, or 1.5 mm defines the viewed scattering volume at 90 degrees and, accordingly, the scattering intensity from rods. The photodetector output signal was analyzed with an ADC converter (L-Card, Russia) and a PC computer. Depending on the pin hole diameter, the particle concentration, and the scattering cross section of GNRs, the setup can operate in an analogue or a photon-counting mode. In the analogue mode, the photocurrent was calculated as the average number of counts for 20 s at an ADC frequency of 5 kHz. In the photon-counting mode, we used special software to convert the ADC output into the number of photons received for 5 min at an ADC frequency of 500 kHz. The instrumental depolarization was measured with 137-nm, 140-nm, and 210-nm polystyrene and 114- and 160-nm silica beads [Fig. S1 in Electronic Supplementary Information (ESI)]. On average, all spectra demonstrate similar behaviour with ~1-2% maxima near the spectral boundaries (at 400 and 900 nm) and 0.5% minima in the central part of the spectra (near 600 nm). Because of the small depolarization ratio expected for small dielectric spheres, the spectra in Figure S1 represent the upper limit of systematic errors for our experimental setup.

In a typical measurement run, the photocurrents I_{VH}^{0} and I_{VV}^{0} were measured for water, and then the photocurrents I_{VH} and I_{VV} were measured for the GNR solution. The depolarization ratio was calculated by $\Delta_{VH} = (I_{VH} - I_{VH}^{0})/(I_{VV} - I_{VV}^{0})$, thus excluding the dark-current contribution from the output data.

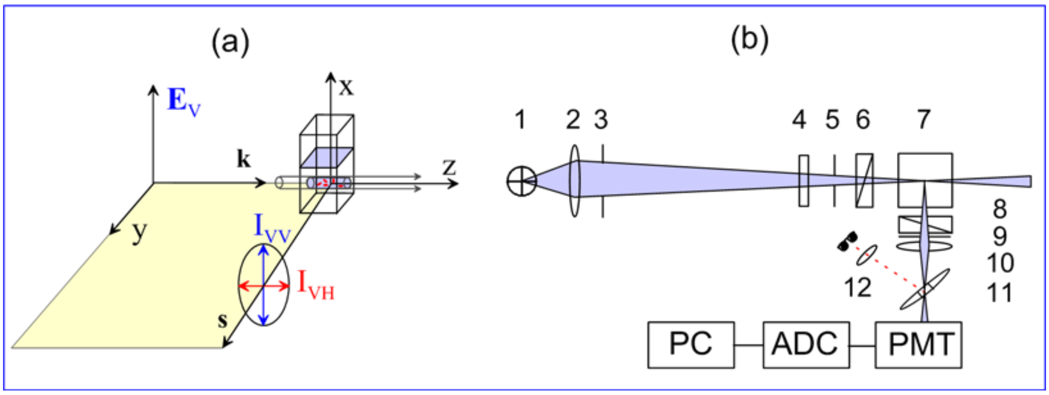

Fig. 1. (a) Scheme for the observation of depolarized light scattering. The incident light propagates in the z-direction and is polarized vertically with respect to the horizontal observation plane (y,z). The scattered co-polarized and cross-polarized intensities are measured at 90° in the y-direction (b) Experimental setup. The numbers stand for a halogen lamp (*1*), achromatic lenses (*2, 10, 12)*, iris diaphragms (*3, 5, 9*), interference filters (*4*) ($\lambda_{\max} = 400 - 1000$ nm, $\Delta\lambda_{1/2,\max} = 5$ nm), a four-sided 1-cm rectangular non-fluorescent-quartz cuvette (*7*), polarization Glan–Thompson calcite prisms (*6, 7*), and a spherical mirror with a pin hole diaphragm (*11*). A spherical mirror (*11*) and lens (*12*) allow for the visual control of scattering volume imaging with respect to the pin hole. The symbols PMT, ADC, and PC designate a photomultiplier (FEU-79, Russia), an analogue-to-digital converter (L-Card Ltd., Russia), and a personal computer, respectively.

2.5. T-matrix calculations

T-matrix calculations were performed as described in detail previously,[30] including the size-corrected optical constants of GNRs and the spectral dependence of the refractive index of water. Specifically, the shape of GNRs was modelled by circular cylinders with the total length L, diameter d, and a variable end-cap geometry described by the end-cap parameter $\chi_c = b/(d/2)$, where b is the end-cap thickness (Fig. 2).

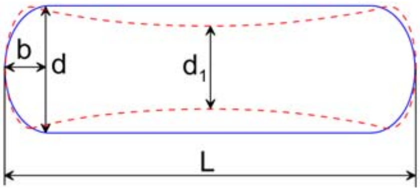

Fig. 2. Geometrical model for a rod with a constant diameter d and an end-cap shape (solid line). The rod's shape is determined by the aspect ratio $r = L/d$ and the end-cap parameter $\chi_c = 2b/d$. For comparison, the dashed line shows the dog-bone model[30] with a reduced central diameter $d_1 = d/(1+\chi_d)$.

Here, $\chi_c = 1$ corresponds to semi-spherical ends, whereas $\chi_c = 0$ corresponds to flat ends. As distinct from the general dog-bone model,[30] the oleate-fabricated nanorods[28] have an almost perfect cylindrical shape with the central diameter d_1 equal to the end-cap diameter $d = d_1(1+\chi_d)$, and the shape parameter $\chi_d = 0$.

For simulations of extinction and depolarization spectra, we used a two-fraction model[26,30] in which the aspect ratio of the major rod fraction was modelled by a log-normal number density distribution,

$$n_{ri} = f_i / \sum f_i = \exp[-\ln^2(r_i / r_{av}) / 2\ln^2(\sigma_r)] / \sum f_i \,, \qquad (1)$$

whereas the impurity particles were modelled by a single fraction of quasi-spherical particles with the average TEM diameter R_s and the aspect ratio r_s. Because of the small polydispersity of our samples, very close results were obtained with a standard normal distribution instead of Eq. (1). The average diameter of rods d_{av}, their aspect ratio r_{av}, the log-normal dispersion parameter σ_r, and the end-cap parameter χ_c

were derived from TEM statistical data. Note that the rod lengths were also distributed with the log-normal number density according to the relationship $L_i = d_{av} r_i$. The ensemble-averaged extinction A_{ext} is defined by the following expression:[30]

$$A_{ext} = \frac{c_g l}{\ln 10 \rho_g V_t}\left[w_R \sum_{i=1}^{n_R} n_{Ri} \langle C_{ext,Ri} \rangle + w_S \sum_{i=1}^{n_S} n_{si} \langle C_{ext,Si} \rangle \right], \quad (2)$$

where c_g is the mass–volume concentration of gold, l is the suspension thickness (here, 1 cm), ρ_g is the density of gold, and V_t is the total volume of all particles per unit volume. In Eq. (2), each i*th* fraction of rods (subscript "R") and impurity quasi-spherical particles (subscript "S") is characterized by the number fractions $n_{Ri} = N_{Ri} / \sum_{i=1}^{n_R} N_{Ri}$ and $n_{Si} = N_{Si} / \sum_{i=1}^{n_S} N_{Si}$, the number concentrations N_{Ri} and N_{Si}, the extinction cross sections $\langle C_{ext,Ri} \rangle$ and $\langle C_{ext,Si} \rangle$, and the total number fractions of rods and impurity particles $w_R = N_R / N = 1 - w_S$ and $w_S = N_S / N$, where $N = N_R + N_S = \sum_{i=1}^{n_R} N_{Ri} + \sum_{i=1}^{n_S} N_{Si}$ is the total number concentration of all particles. In this work, we set $n_S = 1$.

The depolarization ratio Δ_{vh} of randomly oriented particles was calculated by the procedure described in Ref.[26] Briefly, we first calculated the Mueller scattering matrix elements F_{ij}, which transform the Stokes parameters[14] $(I_{\parallel}, I_{\perp}, U, V)$ of the incident light into the corresponding set of scattering Stokes parameters for an arbitrary oriented particle. The averaging over random orientations was performed numerically as described in Refs.,[26,31] and the ensemble averaging of scattering matrix elements was done similarly to that for extinction [see the above Eq. (2)]. The scattering intensities of co-polarized and cross-polarized components are given by $\langle F_{22} \rangle$ and $\langle F_{12} \rangle$, respectively; hence, the depolarization ratio equals $\Delta_{VH} = \langle F_{12} \rangle / \langle F_{22} \rangle$.

For calculation of the extinction spectra, we used analytical averaging formulas.[32] In principle, similar analytical approach could be applied to calculation of the depolarized light scattering spectra by using analytical formulas for the averaged scattering matrix elements.[32] However, for a specific particle size and shape, calculations for each wavelength need recalculating the particle T-matrix. On the other hand, with the calculated T-matrix in hand, the orientation averaging reduces to simple rotation matrix multiplications and summation of data over 100 to 200 orientations. Practically, the main part of spectral calculations for a statistical GNR ensemble is related to the T-matrix calculations rather than to the orientation averaging.

The convergence of double-precision and extended-precision T-matrix codes[30] was checked by comparing the output data for increasing T-matrix orders.[32] Typically, the T-matrix data revealed slow oscillating convergence resembling that for interacting spheres[33,34] and cubes[35] (Fig. S2 in ESI). In general, the maximal relative errors did not exceed 1% for both the extinction and the scattering intensity values.

3. Results and discussion

3.1. Statistical geometric TEM parameters of GNRs

The NaOL + CTAB mixture method[28] has exceptionally broad dimension tunability and can be used for seeded growth synthesis of both thin and thick GNRs of different lengths. Figure 3 shows an overview (a) and an enlarged (b) image of as-prepared GNRs fabricated for a particular set of reagent concentrations that ensure the formation of rods with diameters of about 16 nm and with lengths of about 90 nm. Furthermore, we have found[29] that the same growth solution with NaOL + CTAB can be applied to the fine-tuning of GNR dimensions through an overgrow process in which the originally fabricated GNRs are used as seeds. For instance, Fig. 4 shows an example of GNR-2 overgrown nanorods obtained from the GNR-1 rods seeds shown in Fig. 3. The average diameter of the original GNR-1 rods is increased twofold, and the average length is increased by 30%. Thus, by combining the original method[28] with the overgrowth protocol,[29] one can greatly expand the assessable diameters, length, and aspect ratios of GNRs as compared with one-pot seeded CTAB-mediated growth. For brevity, the as-prepared and overgrown GNRs are subsequently designated GNR-1 and GNR-2, respectively.

To estimate the statistical dispersion in the diameters, lengths, and aspect ratios of GNR-1 and GNR-2, we digitized a representative set of TEM images containing about 600 particles. Figures 5 and 6 show the corresponding statistical histograms for both types of GNRs. The average TEM parameters of the GNR-1 and GNR-2 samples are listed in Table 1.

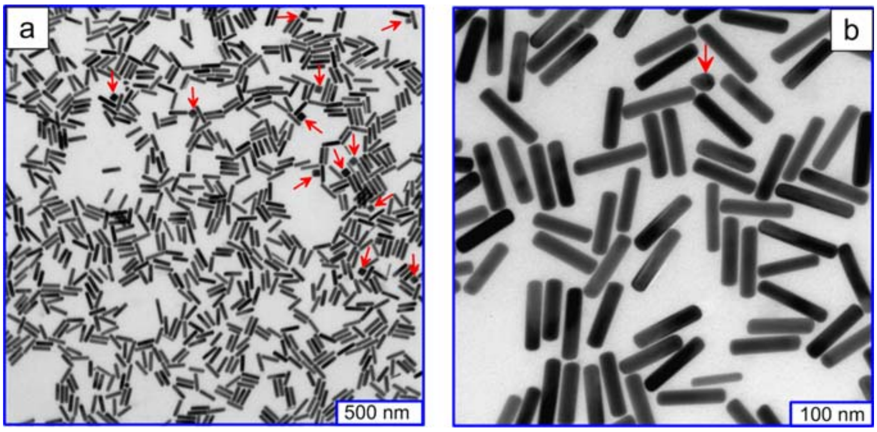

Fig. 3. Overview (a) and enlarged (b) TEM images of GNR-1 nanorods prepared by the NaOL + CTAB method. The arrows point to impurity particles of cubic (a) and quasi-spherical (b) shape.

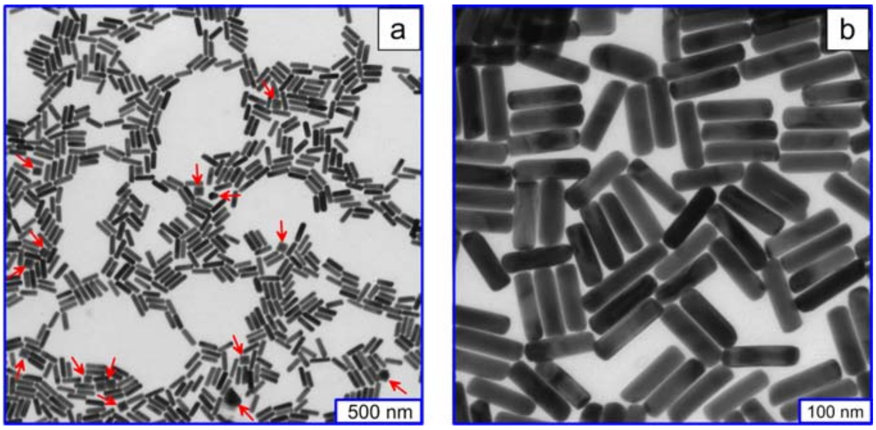

Fig. 4. Overview (a) and enlarged (b) TEM images of GNR-2 nanorods overgrown by the method.[29] The arrows point to impurity particles of cubic and platelet shape (right-bottom corner).

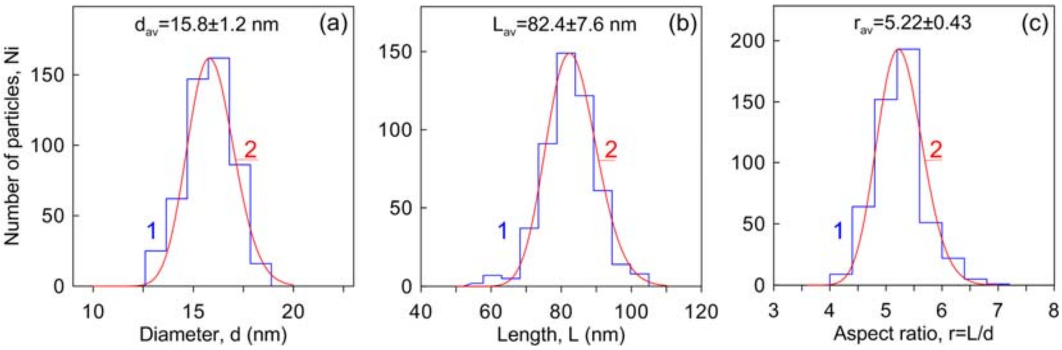

Fig. 5. Statistical histograms (1) and log-normal approximations (2) for the diameter (a), length (b), and aspect ratio (c) of GNR-1. The average values and standard deviations are indicated in the plots.

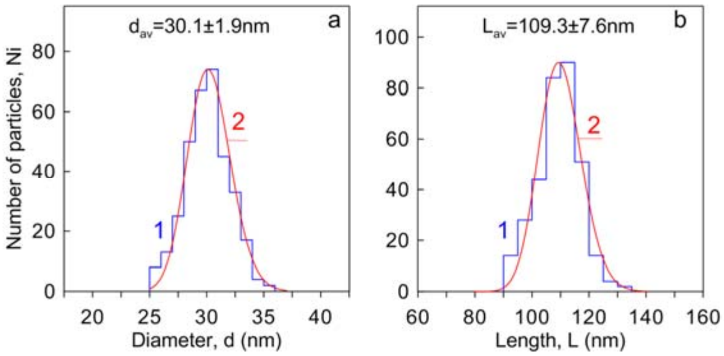

Fig. 6. Statistical histograms (1) and log-normal approximations (2) for the diameter (a), length (b), and aspect ratio (c) of GNR-2. The average values and standard deviations are indicated in the plots.

Table 1. The average TEM parameters of GNR-1 and GNR-2.

Sample	Length, L_{av} (nm)	Diameter, d_{av} (nm)	Aspect ratio, r_{av}	End-cap parameter, χ_c	Radius of impurity particles, R_S (nm)	Percentage of impurity particles, w_S (%)
GNR-1	$82.4 \pm 7.6^*$	15.8 ± 1.2	5.22 ± 0.43	1	16 ± 2	3.1 ± 2.1
GNR-2	109.3 ± 7.6	30.1 ± 1.9	3.63 ± 0.34	0.4	25 ± 3	2.5 ± 2.0

* Standard deviation

The GNR-1 nanorods reveal quite small dimension variations. Specifically, the standard deviations of the average aspect ratio, diameter, and length are 8.2%, 7.6%, and 9.2%, respectively. Such a low dimension polydispersity is not accessible through one-pot CTAB-mediated seeded growth processes.[24] For example, we had to apply an additional separation procedure to achieve an aspect ratio standard deviation of about 16% for CTAB-synthesized GNRs with longitudinal plasmon resonances near 780 nm ($r_{av} = 3.78 \pm 0.54$, $L_{av} = 46.8 \pm 5.2$ nm, $d_{av} = 12.6 \pm 2.3$ nm),[16] 830 nm ($r_{av} = 4.08 \pm 0.72$, $L_{av} = 43.4 \pm 8.2$ nm, $d_{av} = 10.6 \pm 2.2$ nm),[30] and 970 nm ($r_{av} = 5.53 \pm 0.72$, $L_{av} = 60.8 \pm 8.6$ nm, $d_{av} = 11.0 \pm 1.2$ nm).[30] Evidently, the length and diameter distribution of the separated CTAB-fabricated GNRs[16,30] was also broader than those for NaOL + CTAB-fabricated GNR-1 nanorods.

Another instructive example is a study by Liz-Marzán and co-workers,[36] in which a cationic Gemini surfactant (12-EO1-12) was used to prepare monodisperse NRs that were able to form 2D and 3D superlattices. The reported average aspect ratios, lengths, and diameters were $r_{av} = 3.1 \pm 0.4$, $L_{av} = 34 \pm 7$ nm, $d_{av} = 10 \pm 2$ nm for Gem1-GNRs with $\lambda_{\max} = 748$ nm and $r_{av} = 3.9 \pm 0.8$, $L_{av} = 35 \pm 9$ nm, $d_{av} = 9 \pm 2$ nm for Gem1-GNRs with $\lambda_{\max} = 827$ nm.[36] Similar statistical data were reported for CTAB-GNRs[36] based on measuring 1000 particles for each sample. Again, we note that these standard deviations are greater than those obtained for GNR-1 rods. Additional evidence for the excellent monodispersity of GNR-1 and GNR-2 nanorods comes from the broadening of the extinction spectra (see below, sections 3.2 and 3.3).

It should be emphasized that the GNR-2 overgrown nanorods also exhibit excellent monodispersity. By contrast to other overgrowing protocols,[25,37] the NaOL + CTAB-mediated GNR-seeded overgrowth allows fine-tuning to be performed in both perpendicular and longitudinal directions[29] without deterioration of the original GNR-1 monodispersity. It follows from Fig. 6 that the standard deviations of the average aspect ratio, diameter, and length of the overgrown rods are 9.4%, 6.3%, and 7%. Surprisingly enough, these normalized dispersions are close or even smaller that those for the GNR-1 original rods (8.2 %, 7.6%, and 9.2%).

In addition to the small variations in the GNR diameter and length, a remarkable feature of the NaOL + CTAB method is the quite small percentage of impurity particles.[28,29] Specifically, we performed statistical calculations with six overview images containing 900 to 1000 particles each. The average percentage of impurity particles $w_S = N_S / N_R$ and its standard deviation were equal to 3.1 ± 2.1 %. Because of the small number of impurity particles, the standard deviation was about 0.7 of the average value even when a large number of particles (6000) were included in the statistical ensemble (see, e.g., Fig. S4, ESI). This clearly reveals the difficulties related to representative TEM sampling. Nevertheless, the average percentage w_S for non-separated GNR-1 rods was two to three times lower than the similar purity parameter for separated CTAB-GNRs.[16,30]

3.2. Direct problems: Extinction and depolarized light scattering spectra

Figure 7 shows the experimental extinction and depolarization ratio spectra together with the T-matrix calculations based on the TEM statistical parameters of GNR-1 nanorods. The spectral parameters for the GNR-1 and GNR-2 samples are listed in Table 2.

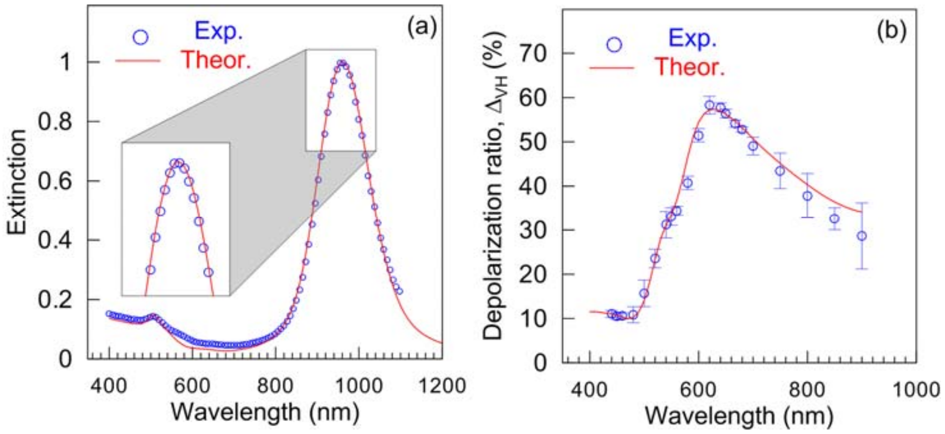

Fig. 7. Experimental (circles) and calculated (solid lines) extinction (a) and depolarized light scattering (b) spectra of GNR-1 nanorods. The T-matrix calculations are based on the average geometrical TEM parameters of the rods (Table 1).

Table 2. The average spectral parameters of GNR-1 and GNR-2 samples.

Sample	Extinction peak position, $\lambda_{\parallel,\max}$ (nm)	Extinction FWHM, (nm)	Δ_{VH} peak position, $\lambda_{VH}^{\max}$ (nm)	$\Delta_{VH}^{\max}$, (%)
GNR-1	968	146	620	59.2 ± 2.5
GNR-2	860	140(120*)	650	53.6 ± 2.0

* FWHM for an as-prepared GNR-2 sample.

In general, the agreement between calculated and measured spectra is almost perfect, except for the slight blue-shifting of the calculated extinction maximum and some deviations in the short-wavelength part of the spectrum below 700 nm. Note that the end-cap shape parameter strongly affects the peak position,[30,38,,39] which shifts to the red for flatter end-caps with $\chi_c < 1$. As the statistical accuracy of $\chi_c = 1$ estimation (Table 1) was not enough, the difference between calculated (950 nm) and measured (958 nm) peak wavelengths can be explained by a slight deviation of the rod end-caps from a hemispherical shape.

Figure 8 shows experimental and calculated extinction and depolarization spectra for overgrown GNR-2 nanorods. In contrast to the GNR-1 samples, the agreement between the measured and calculated extinction spectra of the GNR-2 rods is not satisfactory for either the spectral width or the short-wavelength tail. Besides, the experimental depolarization maximum is somewhat red-shifted and its magnitude is smaller than that of the theoretical maximum. Note that as-prepared GNR-2 rods revealed an even more narrow extinction spectrum with an FWHM of about 120 nm (Fig. S3, ESI); therefore, the difference between TEM-based calculations and measurements is more pronounced as compared with Fig. 8. These differences can be attributed to the insufficient accuracy of TEM sampling (see below). A similar inconsistency between the TEM aspect ratio dispersion and the FWHM of extinction spectra can be seen in the data reported in Ref.[36] Our T-matrix calculations with the reported[36] average aspect ratio, length, diameter, and their standard deviations ($r_{av} = 3.6 \pm 0.4$, $L_{av} = 43 \pm 8$ nm, $d_{av} = 12 \pm 2$ nm) give more broadened spectra as compared with the experimental FWHMs reported in Ref.[36] (132 nm for calculated *vs* 100 nm for experimental spectrum; see Fig. S5a, ESI). A similar or even greater broadening was obtained for Gem1-NRs I and II with LPR wavelengths of 748 and 820 nm, respectively. Specifically, the calculated FWHMs are 132 and 172 nm for Gem1-NRs-I and Gem1-NRs-II, whereas the experimental values are 100 and 126 nm, respectively[36] (see Fig. S5b, ESI).

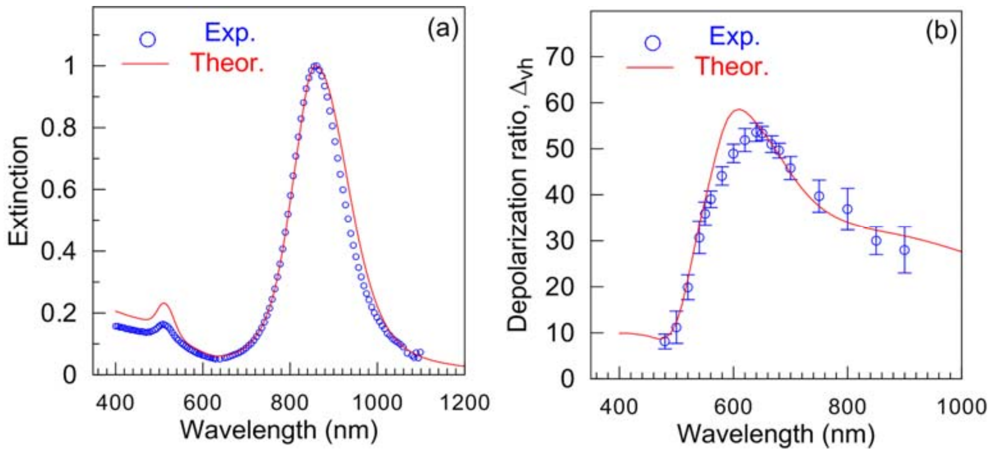

Fig. 8. Experimental (circles) and calculated (solid lines) extinction (a) and depolarized light scattering (b) spectra of overgrown GNR-2 nanorods. The T-matrix calculations are based on the average geometrical TEM parameters of the rods (Table 1).

Consider now some physical mechanisms behind the depolarization spectra. First, we note that the spectral locations of the experimental plasmonic extinction maxima (Figs. 7a and 8a) and depolarization maxima (Figs. 7b and 8b) are quite different. Second, the experimental depolarization maximum (60%) greatly exceeds the upper limit (33%) for dielectric needles[13,14] and is close to the theoretical plasmonic limit of 75%.[15] As these questions have been discussed in previous reports[15,16,40,41] for several approximate models, we now restrict ourselves to a short discussion based on a general theory of scattering by randomly oriented anisotropic molecules or small particles.[42] According to Landau and Lifshitz,[42] the depolarization ratio is given by the expression

$$\Delta_{VH}=\frac{b}{b+a\sin^2\theta}, \qquad (3)$$

where θ is the angle between polarization and scattering vectors [$\sin^2\theta=1-(\hat{\mathbf{e}}_0\hat{\mathbf{k}}_s)^2$]. The constants a and b can be written as linear combinations of scalar (G_0), symmetric (G_s), and antisymmetric G_a invariants of the polarizability tensor α_{ik},

$$a=G_0+\frac{1}{30}G_s-\frac{1}{30}G_a,\quad b=\frac{1}{10}G_s+\frac{1}{6}G_a, \qquad (4)$$

where

$$G_0=\left|\frac{1}{3}\sum_i\alpha_{ii}\right|^2=|\bar{\alpha}|^2,\quad G_s=\sum_{ik}s_{ik}s_{ik}^*,\quad G_a=\sum_{ik}a_{ik}a_{ik}^*, \qquad (5)$$

$$s_{ik}=\frac{\alpha_{ik}+\alpha_{ki}}{2}-\delta_{ik}\bar{\alpha},\quad a_{ik}=\frac{\alpha_{ik}-\alpha_{ki}}{2}. \qquad (6)$$

In the general case, the scattering intensity can be represented as the sum of the scalar, symmetric, and antisymmetric contributions proportional to the corresponding invariants (5). For a symmetric polarizability tensor with $\alpha_{ik}=\alpha_{ki}$ and for our scattering geometry (Fig. 1), Eq. (3) can be written as

$$\Delta_{VH}=\frac{3}{4+30\dfrac{G_0}{G_s}}, \qquad (7)$$

$$G_s=\sum_i|\alpha_i-\bar{\alpha}|^2,\quad \alpha_i\equiv\alpha_{ii}. \qquad (8)$$

For anisotropic dielectric needles, we have $\alpha_2=\alpha_3=0$ and Eq. (7) gives $\Delta_{VH}=1/3$, whereas for thin anisotropic discs, $\alpha_1=0$, $\alpha_2=\alpha_3$ and Eq. (7) gives $\Delta_{VH}=1/8$. In the case of plasmonic rods, the resonance condition[15,40]

$$\bar{\alpha}=0,\quad \alpha_1=-(\alpha_2+\alpha_3) \qquad (9)$$

results in $G_0=0$ and the plasmonic depolarization maximum is $\Delta_{VH}=3/4$.[15] Finally, for axially symmetric particles with $\alpha_2=\alpha_3$, Eq. (7) can be recast in two forms:

$$\Delta_{VH}=\frac{3}{4+5\dfrac{|\alpha_1+2\alpha_2|^2}{|\alpha_1-\alpha_2|^2}}=\frac{\chi^2}{5-2\chi^2}, \qquad (10)$$

where $\chi^2 = |\alpha_1 - \alpha_2|^2 / \left(|\alpha_1|^2 + 2|\alpha_2|^2\right)$. The second form was derived in Ref.[16] and its equivalence to the first expression in Eq. (10) is shown in the ESI file.

To explain the weak wavelength dependence of the depolarization maximum on the particle aspect ratio, we consider spheroidal metallic rods. Then, from the resonance condition (9) we have

$$\operatorname{Re}\varepsilon(\omega) = -\varphi_{VH}\varepsilon_m \, , \qquad (11)$$

$$\varphi_{VH} = \frac{5 - 3L_{\|}}{3L_{\|} + 1} \, , \qquad (12)$$

where $\varepsilon(\omega)$ is the particle dielectric function, ε_m is the dielectric function of the surrounding medium, and $L_{\|}$ is the longitudinal geometrical depolarization factor.[14,42] In Eq. (11), φ_{VH} is equivalent to $2\varphi_{VH}$ in similar conditions in Refs.[5,43] Equation (11) has the same form as the well-known condition for the LPR of different nanoparticles[5,43]

$$\operatorname{Re}\varepsilon = -\varphi\varepsilon_m \, , \qquad (13)$$

where $\varphi = 2$ for spheres and specific forms of φ for nanoshells and homogeneous and layered spheroids can be found in.[43] In particular, for spheroids

$$\varphi_{\|,\perp} = \frac{1}{L_{\|,\perp}} - 1 \, . \qquad (14)$$

The principal difference between the extinction and the depolarization resonance is explained by the different limiting values given by Eqs. (12) and (14). Indeed, for thin rods $L_{\|} \to 0$ and $\varphi_{VH} = 5$, whereas $\varphi_{\|} \to \infty$. Combining Eq. (13) with the Lorenz–Drude formula

$$\varepsilon(\omega) = \varepsilon_{ib} - \frac{\omega_p^2}{\omega^2(1 + i\gamma_p/\omega)} \, , \qquad (15)$$

where ε_{ib} is the interband contribution to the bulk dielectric function of the metal, γ_p is the decay constant and ω_p is the plasma frequency of conductive electrons in the particles, we obtain the resonance wavelength λ_{res} [43,44]

$$\lambda_{res} = \lambda_p \left(\varepsilon_{ib} + \varphi\varepsilon_m\right)^{1/2} \, . \qquad (16)$$

Here, λ_p is the wavelength of electron plasma oscillations (about 131 nm for bulk gold[45]). Thus, with an increase in the aspect ratio, the extinction resonance wavelength goes to far infrared, whereas the depolarization resonance wavelength approaches its limiting value

$$\lambda_{VH}^{\max} = \lambda_p \left[\varepsilon_{ib} + 5\varepsilon_m\right]^{1/2} \approx 610 \text{ nm}, \qquad (17)$$

where the bulk gold material parameters[45] were used for numerical estimation. Thus, Eq. (16) qualitatively explains the quite weak dependence of the depolarization resonance wavelength on the particle aspect ratio. Moreover, the numerical value of 610 nm is in reasonable agreement with the T-matrix simulations and with the experimental observations ($\lambda_{VH}^{\max} \approx 620$ nm).

Because of the mismatch between the plasmonic and the depolarization peak, the scattering intensities of the co-polarized and cross-polarized components at $\lambda_{VH}^{\max}$ are strongly decreased in comparison with their resonance magnitudes at the LPR wavelength $\lambda_{res} = \lambda_{\|}$. Figure 9 shows T-matrix calculations for a polydisperse GNR suspension whose parameters are close to the TEM model for the GNR-1 samples.

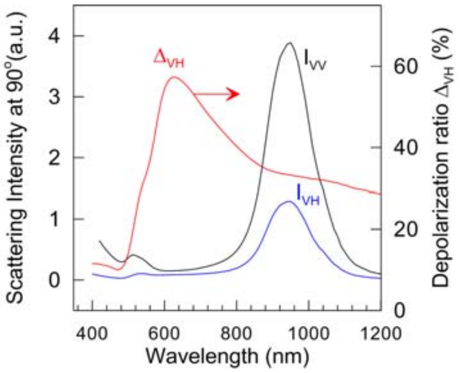

Fig. 9. Spectra of co-polarized $I_{VV}(\lambda)$ and cross-polarized $I_{VH}(\lambda)$ intensities at 90° and the depolarization ratio $\Delta_{VH}(\lambda)$. T-matrix calculations were performed for the TEM parameters of the GNR-1 samples (Table 1 and Fig. 7).

Near the LPR wavelength, the LPR intensity ratio I_{VH}/I_{VV} is about 30% as for thin randomly oriented dielectric needles, whereas at $\lambda_{VH}^{\max}$, this ratio increases to 60%.

It should be emphasized that all our calculations and measurements are for a randomly oriented ensemble. For a single arbitrarily oriented particle (Fig. 10a), the depolarization ratio can vary from 0 to very high values corresponding to some specific orientations.[16,40,41] For example, no depolarization occurs if a rod-like particle is oriented along the x, y, and z axes or if the symmetry axis is located in the (x, y) or (y, z) plane. Thus, we expect the maximal depolarization of light scattered by particles located in the (x, z) plane, when the longitudinal and transversal dipoles are excited in opposite phases.[16,40].

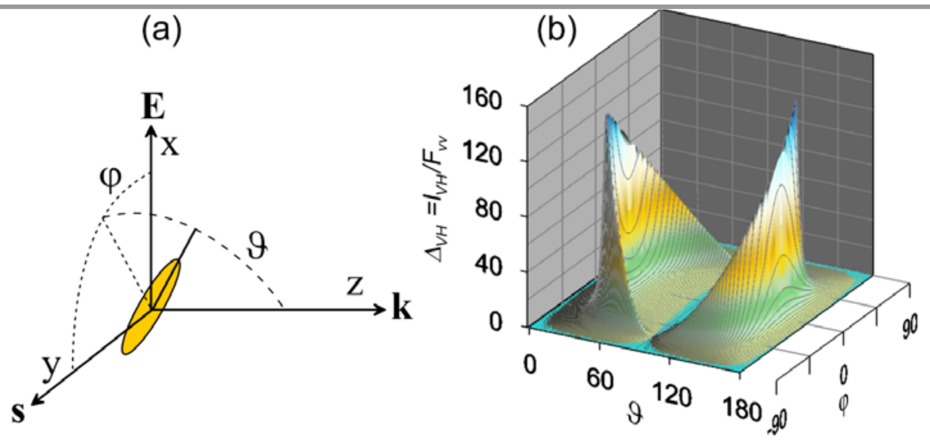

Fig. 10. (a) Scattering geometry in which the incident x-polarized light travels along the positive z direction and the scattered light is observed in the plane (y, z) in the y direction. The arbitrary orientation of a rod-like particle is specified by the ϑ and φ angles. (b) Depolarization ratio as a function of the orientation angles ϑ and φ; T-matrix calculations were performed for GNRs with a length of 80 nm, a diameter of 15 nm, and semi-spherical ends.

This is illustrated by Fig. 10b, in which the depolarization ratio is plotted as a function of the polar and azimuth orientation angles. It follows from the 3D-map in Fig. 3b that, for a constant $\vartheta \approx 20^\circ$ or 160° and for $-45^\circ \le \varphi \le 45^\circ$, the cross-polarized intensity can be 20 to 60 times higher than its co-polarized counterpart. These particular orientations make the major contribution to depolarized light scattering from a randomly oriented ensemble of plasmonic rods.

3.3. Inverse problems: Retrieval parameters from extinction and depolarization spectra

Determining the particle-size distribution (PSD) from extinction and light scattering spectra, angular dependences of the scattered intensity (Mueller matrix elements), or dynamic light scattering (DLS) data is a typical inverse problem in particulate-media optics.[46] Typically, the relationship between the ensemble-averaged optical response and the PSD is formulated as the Fredholm equation of the first kind, which represents an ill-posed problem for inversion.[47] Therefore, various regularization procedures have been developed for the practical inversion of optical, SAXS, and other similar data.[48,49] For example, Peña et al.[50] used a multivariate optimization algorithm to retrieve the PSDs of Au and Cu near spherical particles from their extinction spectra. At present, the DLS technique is widely used to estimate the PSD of nanoparticles[51] because the DLS inversion scheme is not very sensitive to the input optical constants of particles. However, the DLS method is not free from serious drawbacks, discussed, for example, in Ref.[52] In particular, deviation of the particle shape from sphericity can greatly affect retrieval data for the particle size and concentration.[52,53] For nanorod suspensions, the DLS data are difficult to inverse because of the complex shape of the autocorrelation function.[52,54]

The GNR diameter is usually varied within a narrow range, and these variations do not affect the extinction spectra, provided that the upper diameter limit is less than, say, 30 nm.[15,21] By contrast, the longitudinal LPR wavelength depends on the aspect ratio almost linearly and typically varies between 600 and 1200 nm. Accordingly, the FWHM of the extinction spectrum depends strongly on the aspect ratio distribution (ARD),[39] and this property has been exploited by Eustis and El-Sayed[55] to determine the ARD from the Rayleigh–Gans[56,57] approximation. Recently, this approach was extended to use T-matrix calculations.[16,58]

In addition to the extinction spectroscopy of plasmonic particles, Bogatyrev et al.[59] developed a differential light scattering spectroscopy (DLSS) method that was shown to be useful for determining the average particle size or for monitoring the aggregation of functionalized nanoparticles during biospecific interactions.[60] The DLSS method and the suggested setup[59] with minor modifications were recently used by Xu et al.[61] as additional (to the extinction spectra) experimental information for determination of the ARD and concentration of GNRs in samples with a high ARD broadening and a high percentage of impurity particles.

In this section, we describe a simple approach in which the ARD is modelled by a two-parametric log-normal distribution. The average aspect ratio and ARD dispersion are determined from T-matrix calibrations of the extinction and depolarization spectra based on two pre-determined input parameters: the average diameter of rods d_{av} and the end-cap parameter χ_c. Additionally, the average size and percentage of impurity particles are used as fitting parameters together with the depolarization spectra.

The basic steps in our scheme are as follows. We start by determining the extinction peak position and its FWHM, as shown in Fig. 11a. The average diameter of the rods can be easily estimated from TEM images of 10–100 GNRs. Furthermore, it has been shown that the rod thickness does not greatly change the average aspect ratio[15] and the retrieved ARD.[39,58] According to a study by Prescott and Mulvaney,[39] the wavelength maximum is a weak function of the ARD width, whereas the FWHM of extinction spectra increases with an increase in the ARD broadening. Thus, to estimate the average AR, one can use a typical polydispersity parameter σ_r , say 0.1. Then, we can calculate the calibration plot (similar to Fig. 11b) by using first-guess parameters to retrieve the average aspect ratio. Finally, we can improve our first estimation for σ_r by using the calibration plot shown in Fig.11c. In practice, for high-quality samples, a couple of successive iterations are sufficient for the convergent solution shown in Fig. 11.

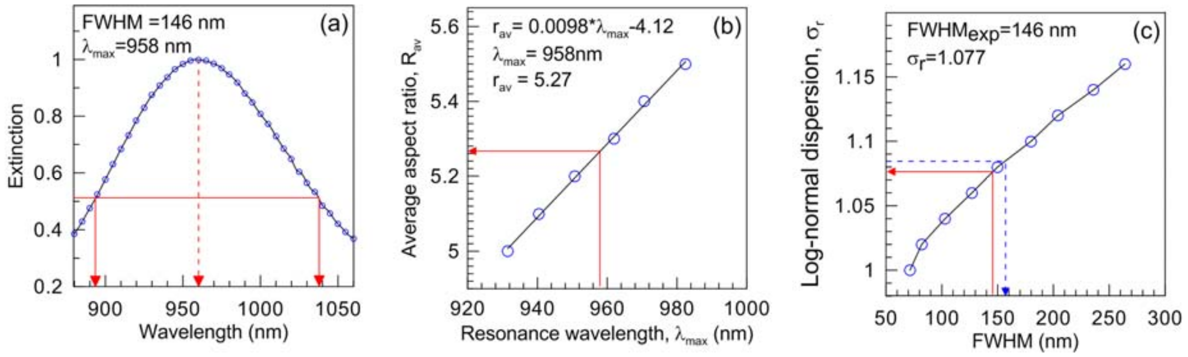

Fig. 11. (a) Determination of the input information for inversion: the peak wavelength and FWHM for the GNR-1 samples. (b) Determination of the average aspect ratio from the plasmonic peak position and the T-matrix calibration plot. (c) Determination of the ARD dispersion parameter σ_r from the FWHM of the extinction spectrum. Calibration plots (b) and (c) were calculated after two successive iterations. Note that the retrieved average AR and ARD dispersion (5.27 and 1.077) are close but not identical to the corresponding TEM estimations. For example, the dashed line in panel (c) indicates an increased FWHM, retrieved from the TEM-based ARD dispersion.

Table 3. TEM and optically retrieved parameters of the GNR-1 and GNR-2 samples.

Sample	Aspect ratio, TEM	Aspect ratio, retrieved	ARD dispersion, TEM (%)	ARD dispersion, retrieved (%)	w_S TEM (%)	w_S retrieved (%)
GNR-1	5.22 ± 0.43	5.27 ± 0.40	1.08	1.08 ± 0.01	3.1 ± 2.1	3.0 ± 0.9
GNR-2	3.63 ± 0.34	3.64 ± 0.45	1.09	1.08 ± 0.01	2.5 ± 2.0	5.0 ± 1.0

Similar solutions to inverse problems were obtained for overgrown GNR-2 rods (Fig. 12). In this case, the difference between retrieved and TEM ARD dispersions is somewhat greater than that for GNR-1 rods. Some TEM and optically retrieved parameters are listed in Table 3.

Estimations of the size and percentage of impurity particles can be done in the same way as described previously in.[16] Therefore, we restrict ourselves here to a short discussion. Figures 13a and b show the experimental extinction and depolarization spectra of GNR-1 nanorods together with T-matrix calculations using TEM or best-fitting parameters for impurity particles. It follows from Fig. 13a that both input data sets give almost identical T-matrix spectra, in close agreement with the measurements. However, the upper 6% value for w_s should be rejected, as it gives a notable decrease in the depolarization maximum. Thus, we conclude that the 3% percentage of impurity particles, as derived from depolarization spectra, is close to the average TEM estimation. This conclusion provides additional strong evidence for the high purity of NaOL GNRs.

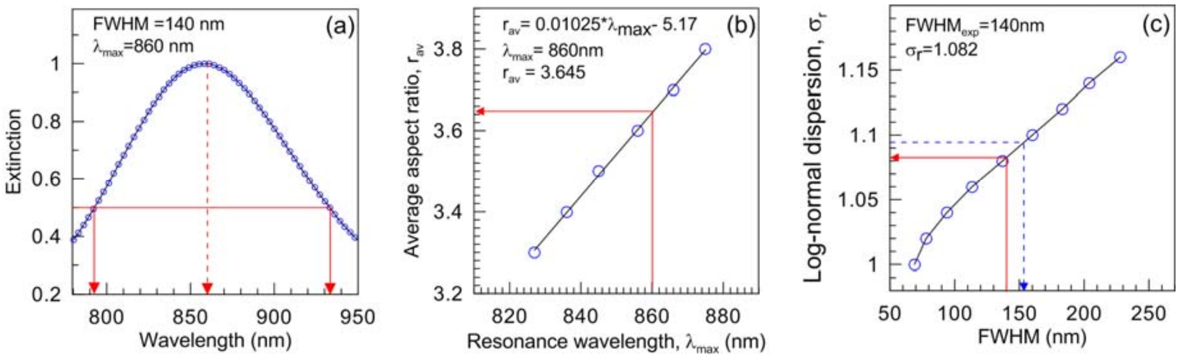

Fig. 12. (a) Determination of the input information for inversion: the peak wavelength and FWHM for the GNR-2 samples. (b) Determination of the average aspect ratio from the plasmonic peak position and the T-matrix calibration plot. (c) Determination of the ARD dispersion parameter σ_r from the FWHM of the extinction spectrum. Calibrations (b) and (c) were calculated after two successive iterations. Note that the retrieved AR and ARD dispersion (3.645 and 1.082) are close but not identical to the TEM estimations (3.63 and 1.094). The dashed line in panel (c) indicates an increased FWHM, retrieved from the TEM ARD dispersion.

Consider now similar spectra for overgrown GNR-2 rods. Again, TEM data give a small percentage $w_S = 2.5$, close to the similar purity parameter for the GNR-1 samples. Looking at the calculated T-matrix spectra for $w_S = 2.5$ and 5% (Fig. 13c), we cannot select the best-fitting value, as both exhibit similar behaviour near the transversal resonance peak. However, the T-matrix depolarization spectra clearly indicate that the lower value of 2.5% should be rejected.

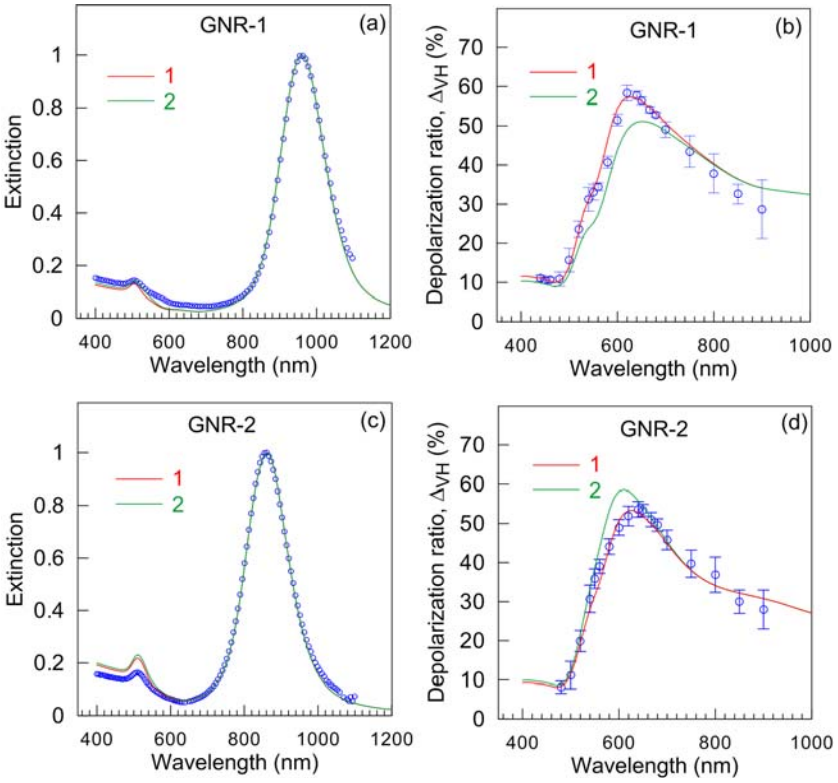

Fig. 13. Experimental (circles) and calculated (solid lines) extinction (a, c) and depolarized light scattering (b, d) spectra of the original NaOL GNR-1 and overgrown GNR-2 nanorods. The red lines (1) correspond to T-matrix calculations with the retrieved best-fitting w_S values listed in Table 3, whereas the green lines (2) show calculations with twofold increased $w_S = 6\%$ (a, b) or decreased $w_S = 2.5\%$ (c, d) percentages of impurity particles.

Thus, by contrast with the initial GNR-1 rods, the optically derived percentage for the overgrown GNR-2 rods is greater than the result estimated by TEM (5% *vs* 2.5%). Of course, even with this increased percentage, GNR-2 suspensions represent a high-quality sample with a low content of impurities, which can be achieved only after special separation of CTAB GNRs.

For GNR-2 sample, the difference between the TEM-measured and the optically-retrieved impurity fractions is statistically significant. However, we cannot improve the agreement between those numbers by simple change of the shape parameter χ_c as such a change results in worse agreement between the measured and calculated extinction spectra. For calculations the depolarization ratio, we used a modified version of Eq. (2), in which the orientation averaged extinction cross-sections were replaced with the Mueller scattering matrix elements $\langle F_{ij} \rangle$. As $\langle F_{ij} \rangle$ are proportional to the squared particle volume V^2 (by contrast to $C_{ext} \approx C_{abs} \sim V$), a small fraction of larger particles could result in a decreased experimental depolarization ratio.

4. Conclusions

In this paper, we have used the binary surfactant NaOL + CTAB mixture[28] to fabricate GNRs with a very low percentage of impurity particles in both as-prepared (<3%) and overgrown (<5%) nanorod samples. It should be emphasized that the same NaOL + CTAB growing system can be successfully used not only for the preparation of high-quality rods but also for an overgrowth process with the initial NaOL + CTAB rods as seeds.[29] Together with the dimensional tunability of the original method,[28] the overgrowth process ensures a flexible dimensional tunability of fabrication technology without any decrease in the sample monodispersity and purity.

With these high-quality nanorods, we have recorded, for the first time, an unprecedented depolarized light scattering ratio of about 60%, which is close to the theoretical limit of 75%. A general analytical treatment for small anisotropic particles explains why the maximal depolarization ratio is observed near 620 nm rather than at the plasmon resonance wavelength. T-matrix calculations for co-polarized and cross-polarized light scattering intensity spectra are in good agreement with the simplified analytical consideration.

Using the TEM geometrical parameters of the rods as the input parameters and T-matrix codes, we have found quite close, though not perfect, agreement between the measured and the calculated extinction and depolarization spectra. It was also found that TEM analysis cannot be considered a convenient and reliable tool to estimate the ARD dispersion and the percentage of impurity particles. By contrast, the plasmonic peak wavelength and the FWHM of an extinction spectrum can be easily inverted into the average aspect ratio and ARD dispersion with the simple calibration curves presented in Figs. 11 and 12. We have shown that the retrieved rod parameters give almost perfect agreement between calculated and measured spectra. Moreover, by combining the extinction and depolarization measurements, one can easily estimate the percentage of impurity particles, as opposed to time-consuming TEM analysis. Our inverse solution, although simple, is not free of any *a priori* information. Specifically, one has to evaluate the average diameter of rods and their end-cap morphology from TEM images. Fortunately, there is no need for thorough statistics, as the average diameter is not a crucial parameter in our inverse scheme. On the other hand, it is possible, at least in principle, to include the light scattering intensity spectra in a more sophisticated inversion scheme so as to make a pure optical estimate of the average rod diameter.[61]

Conflict of interest

The authors declare no competing financial interest.

Acknowledgements

This work was supported by grants from the Russian Foundation for Basic Research (grants 13-02-12413, 12-04-00629-a, 12-02-00379-a, and 11-02-00128-a), the Programs of the Presidium of the Russian Academy of Sciences “Basic Sciences for Medicine” and “Basic Technologies for Nanostructures and Nanomaterials”, and a grant from the Government of the Russian Federation to support scientific research projects implemented under the supervision of leading scientists at Russian institutions of higher education. We thank D. N. Tychinin (IBPPM RAS) for his help in preparation of the manuscript.

Notes and references

[a] Institute of Biochemistry and Physiology of Plants and Microorganisms, Russian Academy of Sciences, 13 Prospekt Entuziastov, Saratov 410049, Russia

[b] Saratov State University, 83 Ulitsa Astrakhanskaya, Saratov 410026, Russia

Electronic Supplementary Information (ESI) available: The ESI file contains short information about the calibration of the depolarization setup, the convergence of T-matrix calculations, and the time-dependent extinction spectra of the GNR-2 samples, as well as overview TEM images of the GNR-1 nanorods, experimental and calculated spectra of

Gem1-NRs, a short theoretical treatment of light scattering by randomly oriented anisotropic particles, and a proof of equivalency of both expressions in Eq. (10). See DOI: 10.1039/b000000x/.

1 M. W. Knight, H. Sobhani, P. Nordlander and N. J. Halas, *Science*, 2011, **332**, 702; M. I. Stockman, *Opt. Express*, 2011, **19**, 22029.

2 L. Vigderman, B. P. Khanal and E. R. Zubarev, *Adv. Mater*., 2012, **24**, 4811; K. M. Mayer, and J. H. Hafner, *Chem. Rev*. 2011, **111**, 3828.

3 R. A. Álvarez-Puebla, E. R. Zubarev, N. A. Kotov and L. M. Liz-Marzán, *Nano Today*, 2012, **7**, 6; P. Negri and R. A. Dluhy, *J. Biophotonics*, 2013, **6**, 20; B. N. Khlebtsov, V. A. Khanadeev, M. Yu. Tsvetkov, V. N. Bagratashvili and N.G. Khlebtsov, *J. Phys. Chem. C*, 2013, **117**, 23162.

4 D. Pissuwan, S. M. Valenzuela and M. B. Cortie, *Biotechnology and Genetic Engineering Reviews*, 2008, **25**, 93; X. Huang, S. Neretina and M. A. El-Sayed, *Adv. Mater*., 2009, **21** 4880; F. Ratto, P. Matteini, S. Centi, F. Rossi and R. Pini, *J. Biophotonics*, 2011, **4**, 64; B. Khlebtsov, E. Panfilova, V. Khanadeev, O. Bibikova, G. Terentyuk, A. Ivanov, V. Rumyantseva, I. Shilov, A. Ryabova, V. Loshchenov and N. Khlebtsov, *ACS Nano*, 2011, **5**, 7077; A. M. Alkilany, L. B. Thompson, S. P. Boulos, P. N. Sisco and C. J. Murphy, *Adv. Drug Delivery Rev*., 2012, **64**, 190; L. Dykman and N. Khlebtsov, *Chem. Soc. Rev*., 2012, **41**, 2256; E. C. Dreaden, A. M. Alkilany, X. Huang, C. J. Murphy and M.A. El-Sayed, *Chem. Soc. Rev*., 2012, **41**, 2740; T. Zhao, X. Shen, L. Li, Zh. Guan, N. Gao, P. Yuan, S. Q. Yao, Q.-H. Xu and G. Q. Xu, *Nanoscale*, 2012, **4**, 7712.

5 N. G. Khlebtsov and L. A. Dykman. *J. Quant. Spectrosc. Radiat. Transfer*, 2010, **111**, 1.

6 H. Chen, L. Shao, Q. Li and J. Wang. *Chem. Soc. Rev*., 2013, **42**, 2679.

7 N. G. Khlebtsov *J. Nanophotonics*, 2010, **4**, 041587.

8 P. R. Evans, G. A. Wurtz, W. R. Hendren, R. Atkinson, W. Dickson, A. V. Zayats, R. Pollard, *Appl. Phys. Lett*., 2007, **91**, 043101.

9 S. Umadevi, X. Feng and T. Hegmann, *Adv. Funct. Mater*., 2013, **23**, 1393.

10 R. Kullock, W. R. Hendren, A. Hille, S. Grafström, P. R. Evans, R. J. Pollard, R. Atkinson and L. M. Eng, *Opt. Express*, 2008, **16**, 21671.

11 P. Zijlstra, J. W. M. Chon and M. Gu, *Nature*, 2009, **59**, 410.

12 J. Sung, M. Sukharev, E. M. Hicks, R. P. Van Duyne, T. Seideman and K. G. Spears, *J. Phys. Chem. C*, 2008, **112**, 3252.

13 M. Kerker, *The Scattering of Light and Other Electromagnetic Radiation*, Academic Press, New York, 1969.

14 H. C. Van de Hulst, *Light Scattering by Small Particles*, Wiley, New York, 1957.

15 N. G. Khlebtsov, A. G. Melnikov, V. A. Bogatyrev, L. A. Dykman, A. V. Alekseeva, L. A. Trachuk, and B. N. Khlebtsov, *J. Phys. Chem. B*, 2005, **109**, 13578.

16 B. N. Khlebtsov, V. A. Khanadeev and N. G. Khlebtsov, *J. Phys. Chem. C*, 2008, **112**, 12760.

17 Z. Gryczynski, J. Lukomska, J. R. Lakowicz, E. G. Matveeva and I. Gryczynski, *Chem. Phys. Lett*., 2006, **421**, 189.

18 J. Pérez-Juste, B. Rodriguez-González, P. Mulvaney and L. M. Liz-Marzán, *Adv. Funct. Mater*., 2005, **15**, 1065.

19 A. M. Zhivkov, B. M. I. Van Der Zande and S. P. Stoylov, *Colloids Surf. A* 2002, **209**, 299; W. Bazhan, K. Kolwas and M. Kolwas, *Opt. Commun*., 2002, **211**, 171.

20 J. A. Reyes-Esqueda, C. Torres-Torres, J. C. Cheang-Wong, A. Crespo-Sosa, L. Rodriguez-Fernandez, C. Noguez and A. Oliver, *Opt. Express*, 2008, **16**, 710.

21 A. V. Alekseeva, V. A. Bogatyrev, B. N. Khlebtsov, A. G. Melnikov, L. A. Dykman and N. G. Khlebtsov, *Colloid J*., 2006, **68**, 661.

22 B. Al-Qadi and T. Saiki, *J. Nanophotonics*, 2009, **3**, 039503.

23. J. Aaron, E. de la Rosa, K. Travis, N. Harrison, J. Burt, M. José-Yakamán and K. Sokolov, *Opt. Express*, 2008, **16**, 2153.

24 Y. Y. Yu, S. S. Chang, C. L. Lee and C. R. C. Wang, *J. Phys. Chem. B*, 1997, **101**, 6661; N. R. Jana, L. Gearheart and C. J. Murphy, *Adv. Mater*., 2001, **13**, 1389; N. R. Jana, L. Gearheart and C. Murphy, *J. Phys. Chem. B*, 2001, **105**, 4065; B. Nikoobakht and M. A. El-Sayed, *Chem. Mater*., 2003, **15**, 1957; C. J. Murphy, L. B. Thompson, D. J. Chernak, J. A. Yang, S. T. Sivapalan, S. P. Boulos, J. Huang, A. M. Alkilany and P. N. Sisco, *Curr. Opin. Colloid In*., 2011, **16**, 128; S. E. Lohse and C. J. Murphy, *Chem. Mater*., 2013, **25**, 1250.

25 K. Sohn, F. Kim, K. C. Pradel, J. Wu, Y. Peng, F. Zhou and J. Huang, *ACS Nano*, 2009, **3**, 2191.

26 A. V. Alekseeva, V. A. Bogatyrev, L. A. Dykman, B. N. Khlebtsov, L. A. Trachuk, A. G. Melnikov and N. G. Khlebtsov, *Appl. Opt*. 2005, **44**, 6285.

27 V. Sharma, K. Park and M. Srinivasaraoa, *Proc. Natl. Acad. Sci. U. S. A*., 2009, **106**, 4981; B. P. Khanal and E. R. Zubarev, *J. Am. Chem. Soc*., 2008, **130**, 12634; O. Akbulut, C. R. MacE, R. V. Martinez, A. A. Kumar, Z. Nie, M. R. Patton and G. M. Whitesides, *Nano Lett*., 2012, **12**, 4060; S. Li, Z. Chang, J. Liu, L. Bai, L. Luo and Sun X. *Nano Res*., 2011, **4**, 723; B. Xiong, J. Cheng, Y. Qiao, R. Zhou, Y. He and E. S. Yeung, *J. Chromatogr. A*, 2011, **1218**, 3823.

28 X. Ye, C. Zheng, J. Chen, Y. Gao and C. Murray, *Nano Lett*., 2013, **13**, 765.

29 B. N. Khlebtsov, V. A. Khanadeev, J. Ye, and N. G. Khlebtsov, *Langmuir*, 2014 (submitted).

30 B. Khlebtsov, V. Khanadeev, T. Pylaev and N. Khlebtsov. *J. Phys. Chem. C*, 2011, **115**, 6317.

31 N. G. Khlebtsov and A. G. Melnikov, *Opt. Spectrosc*., 1995, **79**, 605.

32 M. I. Mishchenko, L. D.Travis and A. A. Lacis. *Scattering, Absorption, and Emission of Light by Small Pparticles*, Cambridge, University Press, 2002.

33 N. G. Khlebtsov, A. G. Melnikov, V. A. Bogatyrev and L. A. Dykman, In *Photopolarimetry in Remote Sensing*, ed. G. Videen, Ya. S. Yatskiv, and M. I. Mishchenko, NATO Science Series, II. Mathematics, Physics, and Chemistry, vol. 161, Kluwer Academic Publishers, Dordrecht, 2004, pp. 265-308.

34 B. N. Khlebtsov, A. G. Melnikov, V. P. Zharov and N. G. Khlebtsov, *Nanotechnology*, 2006, **17**, 1437.

35 M. A.Yurkin and M. Kahnert, *J. Quant. Spectrosc. Radiat. Transfer*, 2013, **123**, 176.

36 A. Guerrero-Martínez, J. Pérez-Juste, E. Carbó-Argibay, G. Tardajos and L. M. Liz-Marzán, *Angew. Chem. Int. Ed*., 2009, **48**, 9484.

37 J. H. Song, F. Kim, D. Kim and P. Yang, *Chem. Eur. J*., 2005, **11**, 910; X. Kou, Sh. Zhang, Zh. Yang, Ch.-K. Tsung, G. D. Stuky, L. Sun, J. Wang and Ch. Yan, *J. Am. Chem. Soc*., 2007, **129**, 6402.

38 N. G. Khlebtsov, L. A. Trachuk and A. G. Melnikov, *Proc. SPIE*, 2004, **5475**, 1; K.-S. Lee and M. A. El-Sayed, *J. Phys. Chem. B*, 2005, **109**, 20331.

39 W. Prescott and P. Mulvaney, *J. Appl. Phys*., 2006, **99**, 123504.

40 N. Calander, I. Gryczynski and Z. Gryczynski, *Chem. Phys. Lett*., 2007, **434**, 326.

41 B. Khlebtsov, V. Khanadeev and N. Khlebtsov, *Phys. Chem. Chem. Phys*., 2010, **12**, 3210.

42 L. D. Landau and E. M. Lifshitz, *Electrodynamics of Continuous Media*, Second ed., Elsevier Butterworth-Heinemann, Amsterdam, 2004.

43 N. G. Khlebtsov, *J. Quant. Spectrosc. Radiat. Transfer*, 2013, **123**, 184.

44 N. G. Khlebtsov, *Quantum Electron*, 2008, **38**, 504.

45 N. G. Khlebtsov, V. A. Bogatyrev, L. A. Dykman and A. G. Melnikov, *J. Colloid Interface Sci*., 1996, **180**, 436.

46 G. Gouesbet and G. Grehan (eds.), *Optical Particle Sizing–Theory and Practice*, Plenum Press, New York, 1988.

47 A. N. Tikhonov and V. Ya. Arsenin, *Solution of Ill-Posed Problems*, Willey, New York, 1977.

48 C. W. Groetsch, *The Theory of Tikhonov Regularization for Fredholm Equations of the First Kind*. Pitman Advanced Pub. Program, 1984.

49 J. Mroczka and D. Szczuczynski, *Appl. Opt*. 2010, **49**, 4591.

50 O. Peña, L. Rodríguez-Fernández, V. Rodríguez-Iglesias, G. Kellermann, A. Crespo-Sosa, J. C. Cheang-Wong, H. G. Silva-Pereyra, J. Arenas-Alatorre and A. Oliver, *Appl. Opt*., 2009, **48**, 566.

51 W. Haiss, N. T. K. Thanh, J. Aveard and D. G. Fernig, *Anal. Chem*., 2007, **79**, 4215.

52 B. N. Khlebtsov and N. G. Khlebtsov, *Colloid J*., 2011, **73**, 118.

53 N. G. Khlebtsov, *Anal. Chem*., 2008, **80**, 6620.

54 B. M. I. van der Zande, J. K. G. Dhont, M. R. Böhmer and A. P. Philipse. *Langmuir*, 2000, **16**, 459; D. Lehner, H. Lindner and O. Glatter, *Langmuir*, 2000, **16,** 1689; M. Pelton, M. Liu, H. Y. Kim, G. Smith, P. Guyot-Sionnest and N. F. Scherer, *Opt. Lett*., 2006, **31**, 2075.

55 S. Eustis and M. A. El-Sayed, *J. Appl. Phys*., 2006, **100**, 044324.

56 D. W. Rayleigh, *Phil. Mag*., 1897, **44**, 28.

57. R. Gans, *Ann. Phys*., 1912, **37**, 881.

58 N. Xu, B. Bai, Q. Tan and G. Jin, *Opt. Express*, 2013, **21**, 2987.

59 V. A. Bogatyrev, L. A. Dykman, Ya. V. Krasnov, V. K. Plotnikov and N. G. Khlebtsov, *Colloid J*., 2002, **64**, 671; V. A. Bogatyrev, L. A. Dykman, B. N. Khlebtsov and N. G. Khlebtsov, *Opt. Spectrosc*., 2004, **96**, 128.

60 N. G. Khlebtsov, V. A. Bogatyrev, L. A. Dykman, B. N. Khlebtsov and Ya. M. Krasnov, *J. Quant. Spectrosc. Radiat. Transfer*, 2004, **89,** 133.

61 N. Xu, B. Bai, Q. Tan and G. Jin, *Opt. Express*, 2013, **21**, 21639.